RBSM Based Analysis on Mechanical Degradation of Non-Air Entrained Concrete under Frost Action – A General Prediction with Various Water Cement Ratio, Lowest Temperatures and FTC numbers

Zhao Wang[a], Fuyuan Gong[b*], Dawei Zhang[b], Yi Wang[c] and Tamon Ueda[d]

[a]*Laboratory of Engineering for Maintenance System, Graduate School of Engineering, Hokkaido University, Japan.*
[b]*College of Civil Engineering and Architecture, Zhejiang University, China.*
[c]*Institute of Industrial Science, University of Tokyo, Japan.*
[d]*Laboratory of Engineering for Maintenance System, Faculty of Engineering, Hokkaido University, Japan.*

Abstract

Frost action is one of the significant factors for deterioration of concrete structures in cold and wet regions. To evaluate the effects of freezing-thawing environment on the structural performance of reinforced concrete structures, it is important to know the degradation of concrete materials such as strength, stiffness, ductility, and so on. In order to investigate the mechanical behaviors of concrete under the effect of frost damage including deformation as well as strength, a two-dimensional mesoscopic Rigid Body Spring Model has been proposed previously. In current paper, a systematic study was conducted to simulate and analyze the frost-damaged concrete. Behavior under mechanical loading including uniaxial compression and tension is simulated on non-air-entrained concrete model after a full process of freezing-thawing cycles is simulated. The deteriorated properties such as compressive strength, tensile strength, elastic modulus, etc. are evaluated and parametric study is conducted. Then, a macroscale prediction model was proposed based on the mesoscale simulation results and it considered different environmental factors which varied among different laboratory experiments. The proposed model could predict the strength degradation in compression and tension of concrete with the number of FTCs which was also verified by numerous experimental results. Besides, pursuant to the existing constitutive models for non-damaged concrete, stress-strain relationships in compression and tension for frost-damaged concrete were developed according to the simulation results and several test data by mathematical regression. Satisfactory correlation was found through the comparisons between analytical and experimental results to show the applicability of the models in studying the structural performance of reinforced concrete structures.

Keywords: concrete; frost damage; rigid body spring model; simulation and modeling

1. Introduction

In cold and wet regions, the reinforced concrete (RC) structures could be damaged due to the freezing-thawing environment. It is rather important to evaluate the structural performance of RC structures under the effect of frost damage to have rational maintenance. It is widely believed that the frost damage of RC structures mainly includes two aspects: the concrete materials and the bond properties between concrete and reinforcement.

In the past decades, many findings were reached by conducting experimental investigations on

the mechanical behaviors of concrete materials under the frost action: On the basis of ASTM C666-84, Shi et al. studied the cylindrical concrete specimens under freezing-thawing cycles (FTC) and an obvious reduction on the compressive strength, tensile strength and elastic modulus was observed for specimens after FTCs [1-2]. Hasan et al. conducted FTC tests through "air-freezing and water-thawing" on concrete prisms [3]. Also, using residual plastic tensile strain as the damage index, an empirical stress-strain model for frost-damaged concrete based on the plasticity and fracture of concrete was proposed. Shang and Song adopted cubic and prismatic concrete specimens with GBJ82-85 FTC test standard, which was similar to ASTM C666 [1, 6], both uniaxial and biaxial behaviors of frost-damaged concrete were tested [4-5]. Duan et al. carried out experiments with unconfined and confined prismatic concrete specimens following GBJ82-85 recommendation [5, 7]. Based on the test results, the degradation models were proposed and FTC numbers were used as the damage index. Zou et al. observed the micro-structures of the frost-damaged concrete prisms by scanning electron microscopy technique and proposed a material degradation model where relative dynamic elastic modulus (RDEM) was chosen as the damage index [8]. Similar with Zou et al., Cao et al. used both FTC number and RDEM as the frost damage index and proposed an empirical deterioration constitutive relationship based on their experimental data [8, 9]. Diao et al. studied the combined effect of steel corrosion, FTC and sustained load on structural performance of RC beams, as well on material properties [10]. However, the minimum temperature of each FTC in Diao et al.'s test was more than two times lower than that in Shang et al. and Duan et al. though they all referred to GBJ82-85 standard [4, 5, 7, 10]. Unlike the FTC process adopted by the above experimental studies, Peterson et al. referred to RILEM TC 176-IDC standard. In their test, only one surface of the specimen was exposed to freezing-thawing environment and the effects of FTC on elastic modulus of concrete and interfacial bond behaviors were studied [11, 12]. In contrast, subjected to the same FTC as Peterson et al., Hanjari et al. experimentally studied the specimens emerged in water [11-13]. Both compressive and tensile degradation of concrete were evaluated, as well as the bond properties after FTCs. All the previous experimental conditions were briefly summarized in **Table 1**. As observed, the test parameters such as concrete mix proportions (eg. water/cement ratio), number of FTCs and minimum temperature of each cycle varied a lot by different researchers. Though some empirical models were proposed to predict the mechanical degradation of concrete, the models were somehow limited to their own test conditions and could hardly be adopted generally [3, 7, 8, 9]. Furthermore, among those tests with air-entrained concrete, quite different results were obtained where some experiments showed almost no strength and stiffness reduction [3, 28] while others showed significant reduction [2, 8]. It indicated that the effectiveness of AEA is very sensitive to the type and quality of AEA. Besides, severe frost damage has been found in many structures even air-entraining-agent was adopted, which yields the effects of AEA is minimal in those structures. Nevertheless, a practical deterioration model for non-AE concrete is still absent at this moment, which is the focus in the current study. The more comprehensive model with the effects of air entrainment would be investigated in the future work, considering the scattered phenomena and uncertainties in different experiments.

In addition to the experimentations, several researches have been conducted to theoretically explain the frost damage of concrete materials: In the beginning, it was believed that the stress causing frost damage was the hydraulic pressure. On basis of Darcy's law, Powers developed the hydraulic pressure model which was a time-dependent approach [14]. Recent studies showed that

the crystallization and cryosuction pressures were another mechanism since frost damage could also be found in partially saturated cases, which could hardly be explained by the hydraulic pressure theory [15]. Coussy and Monteiro developed a static model based on poro-mechanics without considering the hydraulic pressure theory [16]. Gong et al. proposed a comprehensive model combining both Powers' model and poro-mechanical model where the internal pressure during FTC was determined by various environmental factors such as water cement ratio, minimum temperature and so on [17]. The mesoscale Rigid Body Spring Model program has been also developed in the previous studies which could conduct the mechanical simulation of concrete following a full FTC process [18-20]. Compared with the experimental work, the mesoscale simulation approach could not only perform more cases with saving cost and time, but also avoid the artificial errors generated during the tests.

In this paper, mesoscale simulation was conducted on mechanical behaviors of concrete under the effect of frost damage based on the mesoscale Rigid Body Spring Model. Water cement ratio (*w/c*) and minimum temperature of each FTC were set as the variables and the frost damage was evaluated by adopting FTC numbers to a certain degree of damage as the damage index. A prediction model of compressive strength deterioration for frost damaged concrete was developed and it was verified by various available experimental data. In addition, the constitutive relationships including compressive stress-strain and tensile stress-crack width of frost-damaged concrete were also proposed depending on the simulation results and several test data, which could be further utilized in analyzing the structure performance of RC structures under FTC conditions through FEM applications.

Table 1. Review of available experimental studies on frost damaged concrete

	Standard	Size [mm^3]	FTC exposure [℃]	No. of FTCs	*w/c*	Comp. strength [MPa]	Air void [%]	Measured properties[*1]
Shi [2] (1997)	ASTM C666-84	Φ100x203	10→-30 (5 hrs) Min.=-30 (3 hrs) -30→10 (4 hrs)	0, 30, 60, 90	0.35	61.71 59.85	/ (AE)	f_c, E, ν, f_{ts}, τ_s, G
					0.48	43.37 38.63		
Hasan [3] (2004)	ASTM C666-03	100x100x200	20→-25 (1 hr in air[*2]) Min.=-25 (3 hrs in air) -25→15 (1 hr in air) 15→20 (2 hrs)	0, 88, 148, 188	0.60	47.8	4.5 (AE)	ε_{pf}, f_c, E, ε_{c0}
				0, 50, 100, 200, 300	0.50	49.8	1.5[*3]	
Hasan [28] (2002)	ASTM C666-97	100x100x400 100x100x100	4.4~-17.8	0, 34, 62, 109, 205, 261, 305	0.50	Ft=4.43	/ (AE)	RDEM, f_t, E, w_{max}, G_f
				0, 10, 17, 28, 41, 76, 205, 305		Ft=4.20	(Non-AE)	
Zou [8] (2008)	ASTM C666-03	100x100x400	/	0, 100, 150, 200, 250, 300	0.38	42.98	(AE)	f_c, E, ε_{c0}
Shang [4] (2006)	GBJ82-85	100x100x100	6→-15 (2.5-3 hrs) -15→6 (2.5-3 hrs)	0, 25, 50, 75	0.50	34.2	1.7	RDEM, ΔW, f_{ts}, f_c, E, ε_{c0}
Fu [42]	GBJ82-85	100x100x400	8→-17 (1-2 hrs)	0, 25, 50,	0.35	50.7	/	RDEM, ΔW,

(2010)		150x150x150	-17→8 (1-2 hrs)	75, 100, 125	0.39	45.4	(Non-AE)	f_c, f_{ts}, f_t
					0.46	35.6		
					0.58	29.1		
Duan [7] **(2011)**	GBJ82-85	100x100x300	8→-17 (3.5 hrs) -17→8 (3.5 hrs)	0, 50, 75, 100, 125, 150, 175, 200	0.48	41.54	/ (Non-AE)	f_c, E, ε_{c0}, a, b
					0.54	39.18		
					0.60	28.73		
Ji [39] **(2007)**	GBJ82-85	100x100x100	8→-17 (3 hrs) -17→8 (3 hrs)	0, 15, 30, 50	0.5	33.98	1.9	f_c, E, ε_{c0}, f_{ts}
		150x150x150				30.71		
Cao [9] **(2013)**	GBJ82-85	150x150x150	8→-17 (1.5 hrs) -17→8 (1.5 hrs)	0, 25, 50, 75,100, 125	0.41	50.7	3.0	RDEM, f_c, E, ε_{c0}, a, b
					0.44	45.4	3.4	
					0.55	35.6	2.6	
					0.75	29.1	3.0	
Diao [10] **(2011)**	GBJ82-85	100x100x300	20→-35 (2 hrs) -35→20 (2 hrs)	0, 50, 100, 150, 200	0.44	41.30	/ (Non-AE)	f_c, E
					0.50	26.59		
					0.55	26.48		
Peterson [11] **(2007)**	RILEM TC 176-IDC	75x80x250	/	/	0.6	/	1.0	RDEM, E
							1.5	
					0.7		1.5	
Hanjari [13] **(2011)**	RILEM TC 176-IDC	Φ100x200	/	/	0.57	40.97	/ (Non-AE)	RDEM, f_c, E, ε_{c0}, f_{ts}, w_{max}

Note:

[*1]- f_c: compressive strength, E: Elastic modulus, ε_{c0}: compressive peak strain, f_{ts}: splitting tensile strength, f_t: pure tensile strength, τ_s: shear strength, G: shear modulus, RDEM: relative dynamic elastic modulus, ΔW: weight loss, w_{max}: maximum crack width, G_f: fractural energy, a and b: parameters in Guo et al.'s compressive stress-strain model [43];

[*2]-The FTC exposure is "water condition" in default unless "in air" is specifically marked;

[*3]-The air void shown in only number represents "Non-AE" condition;

2. Analytical RBSM Program

2.1 Basic concept of RBSM

The Rigid Body Spring Model (RBSM) is one of the discrete numerical analysis methods. Compared with other discrete numerical methods, RBSM is suitable for the static and small deformation problems such as the cracking issues of concrete materials [19-22]. The concept was firstly brought up by Kawai in 1977 and several discussions were made based on the simulation results of two-dimensional plane stress/strain RBSM programs [23]. Bolander and Saito adopted truss reinforcement elements and concrete elements and applied the approach to analyze reinforced concrete beams [24]. Nagai et al. developed a two-dimensional mesoscale RBSM for concrete materials by introducing mortar elements, coarse aggregate elements and the interfacial transition zone (ITZ) between mortar and aggregate [21]. In the mesoscale RBSM program, the analytical model is divided into polyhedron elements which are randomly arranged using Voronoi diagram to assure that cracks could take place in random directions [18-22]. Each Voronoi cell stands for a mortar or aggregate element and two adjacent elements are connected by a couple of

normal and shear springs. Each element has two translational and one rotational degrees of freedom at the center of gravity, see **Fig. 1**. The values of stiffness for normal and shear springs are calculated as Eq. (1) where a weighted average value is used in case the springs represent mortar-aggregate interfaces [18-22]. In Eq. (1), K_n and K_s mean the stiffness of normal and shear springs; h_i is the length of the perpendicular line from the centroid of element to the boundary, see **Fig. 1**; Naming *Ksp* to be the stiffness with subscripts *n* and *s* standing for normal and shear springs, respectively. The values of *Ksp* could be given as Eq. (2), where E_{elem} and v_{elem} are the mesoscopic elastic modulus and Poisson's ratio of the element (mortar or aggregate) which are derived from the macroscale material values, see Eq. (3) [21].

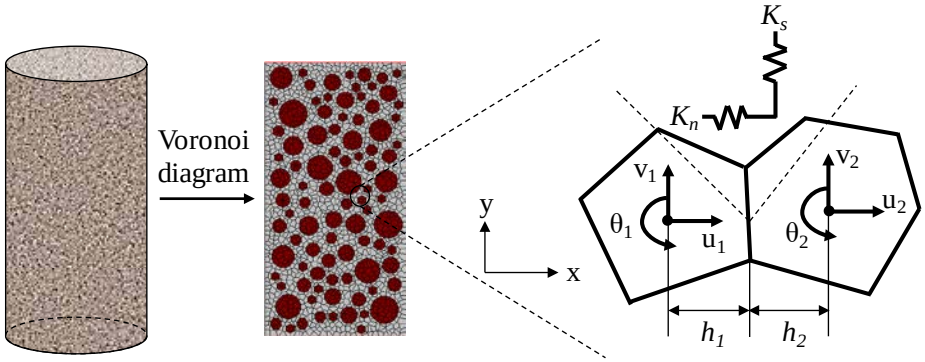

Fig. 1. Schematic diagram of the mesoscale RBSM

$$\begin{cases} K_n = \dfrac{Ksp_{n1}h_1 + Ksp_{n2}h_2}{h_1 + h_2} \\ K_s = \dfrac{Ksp_{s1}h_1 + Ksp_{s2}h_2}{h_1 + h_2} \end{cases} \tag{1}$$

$$\begin{cases} Ksp_n = \dfrac{E_{elem}}{(1 - v_{elem})(1 + v_{elem})} \\ Ksp_s = \dfrac{E_{elem}}{1 + v_{elem}} \end{cases} \tag{2}$$

$$\begin{aligned} v_{elem} &= 20v^3 - 13.8v^2 + 3.8v \\ E_{elem} &= E\left(-8{v_{elem}}^3 + 1.2{v_{elem}}^2 - 0.2v_{elem} + 1\right) \end{aligned} \tag{3}$$

Since concrete is a heterogeneous material, a normal distribution is assumed for the tensile strength of normal springs, see Eq. (4). In which, $f_{t,elem}$ is the tensile strength of the element and assuming $f_{t,elem}=0$ for $f_{t,elem}<0$; μ is the average value of $f_{t,elem}$ while *s* is the standard derivation [21]. For shear springs, an elasto-plastic behavior is adopted where the maximum shear strength τ_{max} is calculated on basis of the state of normal springs, as shown in Eq. (5) [21]:

$$\begin{aligned} f\left(f_{t,elem}\right) &= \frac{\exp\left[\left(f_{t,elem} - \mu\right)^2 / 2s^2\right]}{\sqrt{2\pi}s} \\ s &= -0.2\mu + 1.5 \end{aligned} \tag{4}$$

$$\tau_{\max} = \pm\left(0.11 f_{t,elem}{}^{3}\left(-\sigma + f_{t,elem}\right)^{0.6} + f_{t,elem}\right) \quad (5)$$

in which σ is the normal stress. For the springs of mortar-aggregate interfaces (ITZ), the shear criterion follows:

$$\tau_{\max} = \pm\left(\sigma \tan\theta + c_i\right) \quad (6)$$

where θ and c_i are constant values. When the shear sliding is large enough and the attached length is significantly reduced, the shear stress could decrease. Besides, the shear strength and stiffness could also be affected by the tensile crack width in normal direction. This phenomenon is considering by applying Eq. (7):

$$\begin{aligned} \tau_{\max}{}' &= \tau_{\max}\left(1-\delta_s / l_{elem}\right)\left(1-w / w_{\max}\right) \\ K_s{}' &= K_s\left(1-\delta_s / l_{elem}\right)\left(1-w / w_{\max}\right) \end{aligned} \quad (7)$$

where δ_s and l_{elem} are the sliding distance and length of attaching boundary between the adjacent elements; w is the crack width in normal direction and w_{max} is the maximum crack width for different components. In addition, the tensile stress could also be affected by the shear sliding and a linear reduction is adopted for normal springs in the program as below:

$$\begin{aligned} f_{t,elem}{}' &= f_{t,elem}\left(1-\delta_s / l_{elem}\right) \\ K_n{}' &= K_n\left(1-\delta_s / l_{elem}\right) \end{aligned} \quad (8)$$

The macroscopic material properties are input referring to the previous researches where some values have been proved to be related with others. If one parameter is given, the rest ones could be calculated, see Eq. (9) [21].

$$\begin{cases} E_m = 1000\left[7.7\ln\left(f_{cm}{}'\right) - 5.5\right] \\ f_{tp} = 1.4\ln\left(f_{cm}{}'\right) - 1.5 \\ c / w = 0.047 f_{cm}{}' + 0.5 \\ c_i = -2.6 w / c + 3.9 \\ f_{ti} = -1.44 w / c + 2.3 \end{cases} \quad (9)$$

where f_{cm} is the compressive strength of mortar; E_m is the elastic modulus of mortar; f_{tp} is the pure tensile strength of mortar; f_{ti} is the tensile strength of ITZ; w/c is the water cement ratio and c_i is the parameter in interface criterion (see Eq. (6)). Eq. (9) yields that ITZs have lower strength than mortar since f_{ti} is always less than f_{tp}.

2.2 Frost damage model in RBSM

2.2.1 Ice content evaluation

Ice content is a very important factor to evaluate the frost damage of cementitious materials. Moreover, to accurately estimate the ice content, the freezing point of pore water and pore size distribution of the porous materials should be known.

The freezing points of water in pores with specific radius (r_0) could be calculated based on Eq. (10) where $\gamma_{CL}\approx 0.04 J/m^2$ is the specific energy of crystal/liquid surface; $\Delta S_{fv}\approx 1.2 J/cm^3K$ is the molar entropy of fusion; T_0 is for certain freezing temperature in Kelvin unit; $\delta\approx 0.9nm$ is the

thickness of liquid film between the ice crystal and the pore wall [15, 17, 25].

$$r_0 = -\frac{2\gamma_{CL}}{T_0 \Delta S_{fv}} + \delta \tag{10}$$

In previous studies, the authors have proposed an empirical pore size distribution model based on the water adsorption test by Xi et al. [26]. The model considers a wide range of parameters such as water/cement ratio, curing age and curing temperature etc., as shown in Eq. (11):

$$\begin{aligned} V(r \geq r_0) &= \frac{\left(W_{sat} - W(r_0)\right)/\rho_{wat}}{1/\rho_{solid} + W_{sat}/\rho_{wat}} \\ &= \frac{1/\rho_{wat}}{1/\rho_{solid} + W_{sat}/\rho_{wat}} \left\{ W_{sat} - \frac{CkV_m(RH)}{\left[1-k(RH)\right]\left[1+(C-1)k(RH)\right]} \right\} \end{aligned} \tag{11}$$

where $V(r \geq r_0)$ means the absolute volume of pores with larger radius than r_0 in unit volume of cement paste; W_{sat} stands for the normalized water content by weight of cement paste; ρ is the density of substance; RH is the relative humidity; The values of W_{sat} and RH could be calculated as Eq. (12) in which $\gamma_{LV} \approx 0.072 \mathrm{J/m^2}$ is the specific energy of liquid/vapor surface; $v_l = 1.8 \times 10^{-5} \mathrm{m^3/mol}$ is the molar volume of water; $R = 8.314 \mathrm{J/K/mol}$ is the ideal gas constant; $\delta' = 10^{-9}\left(0.834RH + 0.626 + 0.02309(1.105 - RH)^{-1}\right)$ is the thickness of adsorbed liquid-like layer [27]. The other parameters are given in Eq. (13) based on Xi et al. [26].

$$\begin{aligned} W_{sat} &= \frac{CkV_m}{(1-k)(1+(C-1)k)} \\ RH &= \exp\left(-\frac{2\gamma_{LV}}{r_0 - \delta'}\frac{v_l}{RT}\right) \end{aligned} \tag{12}$$

$$\begin{cases} V_m = 0.9\left(0.068 - \dfrac{0.22}{t}\right)\left(0.85 + 0.45\dfrac{w}{c}\right) \\ k = \dfrac{(1-1/n)C - 1}{C-1} \\ n = 1.1\left(2.5 + \dfrac{15}{t}\right)\left(0.33 + 2.2\dfrac{w}{c}\right) \\ C = \exp\left(\dfrac{855}{T}\right) \end{cases} \tag{13}$$

In Eq. (13), t is the curing age; T is the curing temperature in absolute unit and w/c is the water cement ratio. Combining Eq. (10) and (11), the ice content at a certain temperature could be calculated by integrating the normalized pore size distribution $v(r \geq r_0)$. To consider and quantify the phenomenon of hysteresis between freezing and thawing, the pore shape factor is adopted since the freezing point is usually controlled by the size of pore entry while the thawing point is usually controlled by the size of pore body [17, 18, 30]. The pore shape factor ζ could be approximately regressed by the minimum temperature of FTC as $\zeta = -0.0095T_{min} + 0.125$ according to Gong et al. [18] based on Sun and Scherer's tests [30]. The thawing curve is modified as following: in the relationship between ice content and temperature, if temperature has reached the minimum T_{min} and starts to increase, the existing ice will not melt immediately but melt until the temperature reaches ζT_{min}. Eq. (10-13) show that the ice content is affected by both w/c (assuming

constant degree of hydration), temperature and RH or degree of saturation.

2.2.2 Internal pressures during FTC

It has been widely agreed that multi pressures would initiate during the FTC process. To explain the contradictory experimental phenomenon in closed and open tests [28, 29], the authors have proposed a more comprehensive internal pressure model by combining the hydraulic pressure model and the cryosuction/crystallization pressure model.

For the hydraulic pressure, both water flow theory (Powers) and poro-mechanical theory of volume expansion (Coussy and Monteiro) are taken into consideration [14, 16, 17]. The expression of hydraulic pressure P_h is shown in Eq. (14). More detailed introduction could be found in Gong et al. [17].

$$0.09\varphi\dot{\psi}_c - \frac{A}{V}\frac{m}{\eta}\frac{2}{R_E - r_E}P_h = \left(\frac{b}{K_p} + \frac{\varphi\psi_c}{K_c} + \frac{\varphi\psi_l}{K_l}\right)\dot{P}_h \tag{14}$$

where φ is the porosity; m is the permeability of the porous body; η is the viscosity of liquid water; K is the bulk modulus with subscripts p, c and l for porous body, ice content and liquid, respectively; b is the Biot coefficient; r_E and R_E are the equivalent radii of air void and influential radius (average spacing factor between air voids $L = 2R_E$); A and V are the equivalent empty space and influential volume; ψ represents the volume fraction in pore space with subscripts l and c standing for liquid and ice.

Due to the effect of surface tension, pressure difference exists on crystal-liquid surface and liquid-vapor surface, which result in the cryosuction pressure P_l, see **Fig. 2**. Assuming the pressure of vapor is same as ambient pressure (zero), the cryosuction pressure is always negative. The pressure uniformity of liquid requires that the surface tension of liquid-crystal interface is equal to that of vapor-liquid interface, which yields "$\kappa_{CL}\gamma_{CL}=\kappa_{LV}\gamma_{LV}$" where κ and γ are the curvature and specific energy of interface between different phases, subscripts CL and LV stand for the liquid-crystal interface and vapor-liquid interface. Besides, it indicates that $\kappa_{CL}\gamma_{CL}=\Delta S_{fv}(T_0-T)$ by Scherer [15, 18] so that cryosuction pressure can be calculated from temperature as Eq. (15) depending on the liquid content. Accompanied with the cryosuction pressure, the crystallization pressure P_c acts on the pore wall which depends on the shape of the pores [18, 30], see **Fig. 2**. The formulas to calculate crystallization pressure is also given in Eq. (15) where ζ is the pore shape factor. As mentioned in section 2.2.1, the ice content (ψ_c) could be affected by water cement ratio of the porous materials and temperature, thus the internal pressures would also vary with these factors.

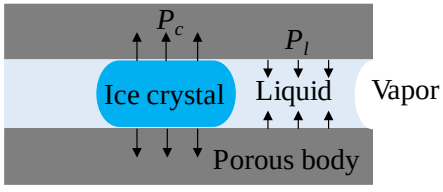

Fig. 2. Cryosuction and crystallization pressure in a cylindrical pore

$$P_l = \psi_l \Delta S_{fv} (T - T_0)$$
$$P_c = -\psi_c (1-\zeta) \Delta S_{fv} (T - T_0) \quad (15)$$

2.2.3 Constitutive laws for porous body with ice

For a porous body when ice forms and internal pressures initiate, the stress-strain relationship of the springs in RBSM can be modeled. Ueda et al. developed a linear unloading and reloading path after the maximum historical strain reaches ε_0, see the red lines in **Fig. 3** and **4** [22]. The compressive strain ε_{pa} could be calculated based on the experimental data [22, 31]. It should be noted that two systems exist in the frozen cementitious material: the porous body system and ice-liquid system. The effective internal pressure due to ice formation $\sigma_0 = b(P_h + P_l + P_c)$ would take place firstly in the ice-liquid system. With expansion of the porous body, this effective pressure would be released until an equilibrium is achieved between the two systems, as the intersection point in **Fig. 3**. For convenience of the simulation, the internal pressure could be applied externally on the combined systems of ice-liquid system and porous body system instead of internally on the ice-liquid system, see **Fig. 4** as long as the final stress (σ_p) and strain (ε_{ta}) of porous body are same [17, 19, 20].

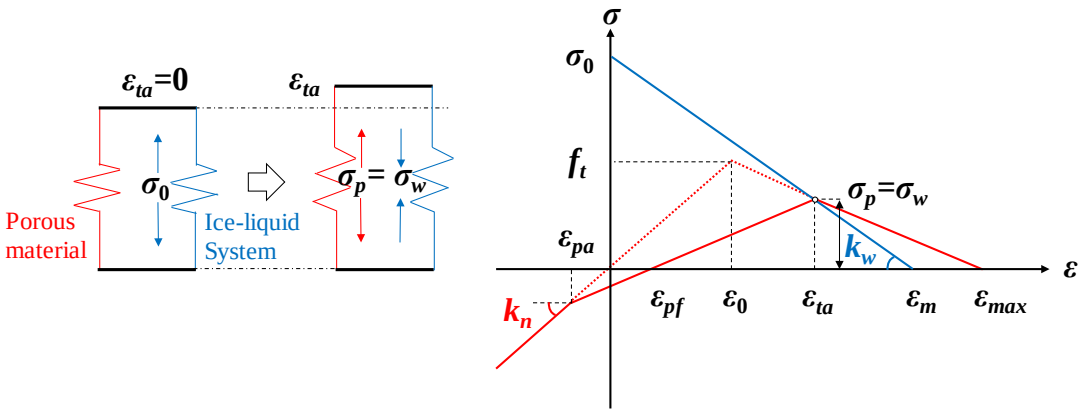

Fig. 3. Internal pressure applied internally on ice-liquid system

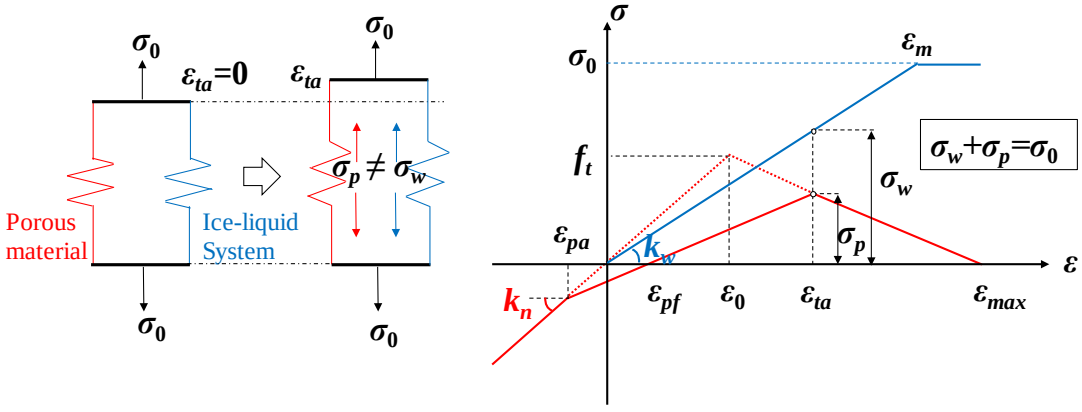

Fig. 4. Internal pressure applied externally on ice-liquid system and porous body system

3. Mesoscale Simulation

In order to analyze and model the mechanical behavior of concrete under the effect of frost damage, two-dimensional concrete specimens were modeled and simulated with RBSM. The dimension of models was 100x200 mm^2 with coarse aggregates occupying around 40% of the volume. The number of coarse aggregates was calculated according to the grain size distribution by JSCE standard [18-21]. Mesh size was set to be around 3mm and total number of the elements was approximately 2600 (see **Fig. 1**).

Material inputs could be adopted by Eq. (9) where the parameters were given based on water cement ratio in the current study. It should be noted that the values of elastic modulus of aggregate E_a, Poisson's ratio of mortar v_m, Poisson's ratio of aggregate v_a were set respectively to be constant values which equaled to 50GPa, 0.18 and 0.25 while he frictional angle in shear criterion of ITZ (in Eq. (6)) was set a typical value of 35° [21]. All models were assumed to be fully saturated. As an important factor for frost damage, the porosity which would affect the hydraulic pressure (see Eq. (14)) could be calculated by water cement ratio [32]: since the normalized water content by weight of cement paste W_{sat} was given in Eq. (16), the total volume ratio of pores in cement paste φ_{cp} and mortar φ_m (neglecting the pore volume in ITZ) would be:

$$\varphi_{cp} = \frac{W_{sat} / \rho_{wat}}{1/\rho_{solid} + W_{sat} / \rho_{wat}} \qquad \varphi_m = f_{cp} \varphi_{cp} \tag{16}$$

where f_{cp} was the volume fraction of cement paste in mortar which could be determined by:

$$f_{cp} = 1 - f_{sand} = 1 - \frac{m_{sand} / \rho_{sand}}{m_{sand} / \rho_{sand} + m_{wat} / \rho_{wat} + m_{cem} / \rho_{cem}} \tag{17}$$

Here a linear relationship between f_{cp} and w/c was proposed depending on Sicat et al.'s experiment where f_{cp}=0.313w/c+0.486 [31, 32]. Combining Eq. (9), (16) and (17), all the necessary material values could be calculated. The effect that non-uniform porosity and thickness of ITZ due to bleeding and gravity might affect the frost damage was neglected since the thickness of ITZ was assumed to be zero in the Rigid Body Spring Model for simplicity.

As mentioned above, the water cement ratio (w/c) and minimum temperature of each FTC ($T_{\min}$) would mainly affect the degradation of concrete by affecting the ice content and thus internal pressure. Thus, w/c and $T_{\min}$ were determined as the simulation variables while the frost damage was controlled and evaluated by the number of freezing-thawing cycles (N). Considering the most adopted cases in laboratory tests and engineering applications, three types of concrete model were prepared with different water cement ratio (0.4, 0.5 and 0.6). The material inputs for concrete models were calculated based on Eq. (9), (16) and (17) and they were listed in **Table 2**.

Table 2. Material inputs for concrete models with different *w/c*

w/c	f_{cm}' [MPa]	E_m [MPa]	f_{tp} [MPa]	f_{ti} [MPa]	c_i [MPa]	φ_m
0.4	42.55	23380.81	3.75	1.72	2.86	0.179
0.5	31.91	21165.66	3.35	1.58	2.60	0.217
0.6	24.82	19230.54	3.00	1.44	2.34	0.257

For each frost-damaged concrete model (with specific material inputs), simulation of entire

process of FTC (with specific minimum temperature T_{min} and number of cycles N) was conducted first. Afterwards, the behavior of frost-damaged model under mechanical loading including uniaxial compression and tension was simulated. Finally, parametric study was conducted on basis of the simulation results. For each type of model, five cases of FTC were adopted depending on the minimum temperature of each cycle (-10, -15, -20, -30 and -40 ℃) and the FTC stopped at 50, 100, 150, 200 and 300 cycles, respectively. Besides, a reference model without frost damage was simulated for comparison. It should be emphasized that in this simulation, the temperature and moisture contents were assumed to be uniform inside the model. In other words, no considerations on heat and moisture transfer were taken in current study and the damage took place uniformly despite of the locations [20]. Besides, previous studies indicated that there was no obvious difference whether the freezing and thawing rate were considered pertaining to the final status of frost-damaged concrete [18-19]. To achieve faster computation speed for consideration of the large amount of simulation cases, simplification with neglecting the freezing and thawing rate was adopted. After FTC ended, the models were tested with compression and pure tension in which prescribed displacement loading was applied on top surface of the model while bottom surface acted as the supporting edge. Loading speeds for compression and tension were set 0.005mm/step and 0.001mm/step respectively. For other boundary conditions, horizontal and rotational restraints were given to both loading and supporting surfaces.

4. Results and Analysis

4.1 Residual strain and meso-cracks after FTC

After frost damage, the models would show unrecoverable plastic tensile deformation due to the meso-cracks, which was also observed in many previous experiments [3, 28, 29, 31]. For instance, **Fig. 5** showed the vertical strain of C0.5-20 model suffering 300 freezing-thawing cycles and the meso-cracks illustration at the end of 200th cycle. In **Fig. 5**, the short red lines meant that 0.005mm wide meso-cracks had occurred in the corresponding normal springs. Since ITZ usually acted as the weakest part in concrete, meso-cracks would initiate in the ITZ part earlier than in the mortar part, which could be seen in **Fig. 5**. For some structural analysis on frost damaged RC structures such as experiment or FEM approach, the residual plastic tensile strain might be measured or given as an index to evaluate the frost damage degree [3, 33]. Besides, almost no material tests on frost-damaged concrete had showed the information of residual strain after FTC [2, 7-9]. As a results, the simulated values of residual tensile strain were also given, see **Table 3**.

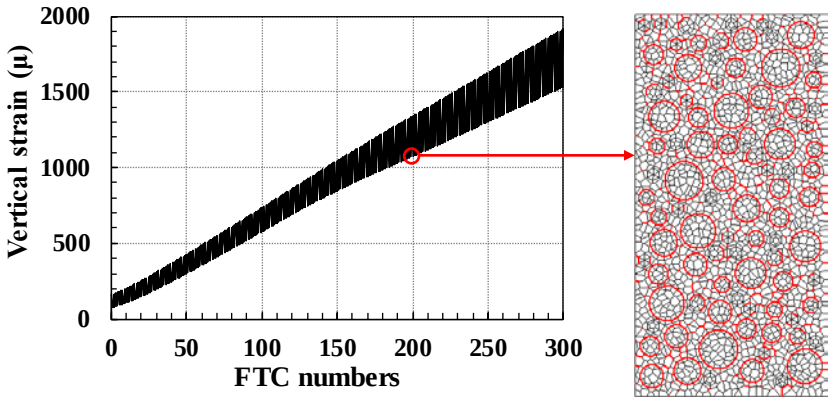

Fig. 5. Vertical strain during 300 FTCs and meso-crack propagation (0.005mm)

Table 3. Residual tensile strain for all the models (μ)

Model	*w/c*	T_{min} (℃)	FTC Numbers				
			50	**100**	**150**	**200**	**300**
C0.4-10	0.4	-10	0.01	0.12	10.39	77.85	390.77
C0.4-15		-15	7.48	68.03	203.61	380.09	741.28
C0.4-20		-20	108.30	273.95	455.48	638.06	976.03
C0.4-30		-30	353.31	536.77	729.90	891.98	1208.73
C0.4-40		-40	430.76	621.81	793.96	954.33	1264.24
C0.5-10	0.5	-10	0	10.59	132.01	388.44	932.22
C0.5-15		-15	56.54	265.34	540.19	813.71	1290.58
C0.5-20		-20	305.12	578.84	847.09	1083.16	1528.94
C0.5-30		-30	621.61	892.29	1106.80	1354.76	1795.19
C0.5-40		-40	725.30	970.76	1186.92	1421.88	1865.34
C0.6-10	0.6	-10	0.21	92.62	440.41	828.19	1470.63
C0.6-15		-15	183.01	560.34	921.58	1200.44	1872.15
C0.6-20		-20	533.18	904.39	1231.07	1545.35	2174.17
C0.6-30		-30	903.83	1223.22	1527.38	1843.16	2229.35
C0.6-40		-40	985.54	1308.04	1608.42	/	/

4.2 Degradation of compressive behaviors

The simulation results of the compressive strength were listed in **Table 4** from which it could be indicated the compressive strength of concrete diminished obviously with increasing numbers of FTC, lower temperature cycles and larger water cement ratio. **Fig. 6** showed the compressive stress-strain curves of C0.5-20 series after suffering different numbers of FTC, the cracking failure pattern and deformation at post peak stage. In **Fig. 6**, the short red lines meant that the strains of normal springs had reached ε_{max} which made the normal springs ineffective (see **Fig. 3** and **4**) and the deformation had been enlarged by 10 times. From **Fig. 6**, it yielded the compressive strength (f_c) would decrease with accumulation of frost damage while the compressive strain at peak stress (ε_c) would show continuous increase. Besides, with more FTCs, the stiffness showed obvious diminishment but "stiffness recovery" effect existed for the frost damaged concrete: the stiffness of frost damaged concrete would perform a reduced value at first owing to the meso-cracks by FTC but later show a higher value with crack closing. This phenomenon was also observed and explained by several experimental studies, such as Hasan et al., Zou et al., Duan et al. and Cao et al. etc. [3, 7-9].

Table 4. Compressive strength for all the models (MPa)

Model	*w/c*	T_{min} (℃)	FTC Numbers					
			0	**50**	**100**	**150**	**200**	**300**
C0.4-10	0.4	-10	30.88	29.93	29.83	28.94	30.14	27.39
C0.4-15		-15		31.22	32.01	27.87	30.43	25.52

C0.4-20		-20		30.11	30.36	25.80	24.29	19.97
C0.4-30		-30		27.78	24.09	23.49	19.71	15.51
C0.4-40		-40		27.00	24.65	21.64	19.07	15.52
C0.5-10		-10		25.49	23.00	24.40	22.09	13.78
C0.5-15		-15		26.21	23.52	20.01	14.69	11.21
C0.5-20	0.5	-20	24.98	23.89	20.57	16.44	12.01	8.99
C0.5-30		-30		20.73	14.36	12.75	10.45	7.23
C0.5-40		-40		20.49	13.13	12.86	10.26	6.58
C0.6-10		-10		20.00	18.72	17.94	14.28	7.51
C0.6-15		-15		18.85	16.05	10.40	11.98	5.34
C0.6-20	0.6	-20	21.20	16.39	12.13	9.97	7.31	4.34
C0.6-30		-30		12.15	8.3	7.16	5.71	4.43
C0.6-40		-40		10.71	7.80	7.15	/	/

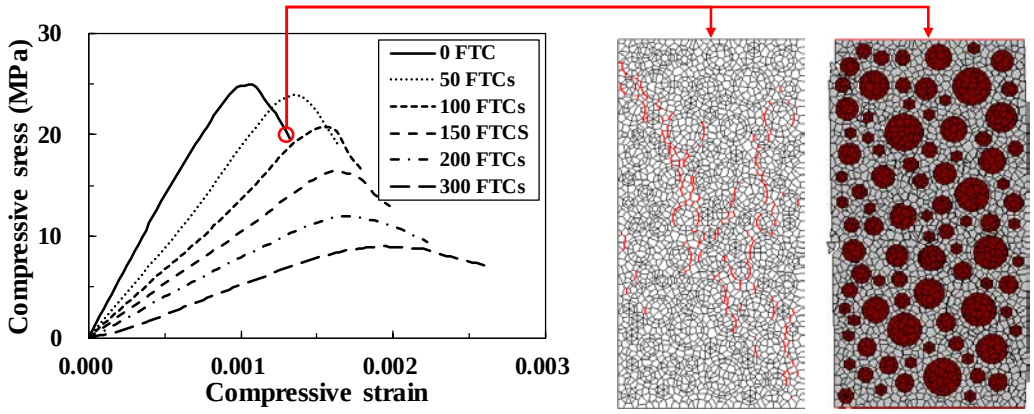

Fig. 6. Stress-strain relationship for C0.5-20 series, cracking failure pattern and deformation

In order to model the deterioration of compressive strength for frost damaged concrete, Berto et al. adopted an environmental damage parameter d_{env} (=1-f_{cd}/f_c) where f_c and f_{cd} stood for the compressive strength of sound and damaged concrete, see Eq. (18) [34]. The environmental damage parameter d_{env} could be calculated based on Eq. (19) if considering ASTM C666 (A) frost damage condition [34-35]. In Eq. (19), λ was a parameter depending on the compressive strength of sound concrete f_c; N_{eq} was called the equivalent number of FTCs on basis of ASTM C666 (A) condition which could be calculated depending on the actual number of FTCs-N, as shown in Eq. (20) [34]:

$$d_{env} = 1 - \frac{f_{cd}}{f_c} \tag{18}$$

$$d_{env} = \lambda N_{eq} \tag{19}$$

$$N_{eq} = \chi N^{\beta} \tag{20}$$

in which χ and β were parameters depending on experimental conditions. Substituting Eq. (18) and (20) into Eq. (19) and letting $\alpha=\chi\lambda$, the relative compressive strength Rf_c (=f_{cd}/f_c) would be expressed as Eq. (21) where α and β were parameters relating to concrete strength (w/c) and FTC

conditions (w/c, T_{min}). Through fitting the simulation results with Eq. (21), it was found that compressive strength showed approximately linear reduction with the numbers of FTC thus β could be adopted with 1.0. α could be determined by water cement ratio w/c and minimum temperature $T_{\min}$, as shown in Eq. (22):

$$Rf_c = 1 - \alpha N^{\beta} \tag{21}$$

$$\alpha = \left[\left(1.5\frac{w}{c} + 0.6\right)\ln\left(-T_{\min}\right) + \left(6\frac{w}{c} - 5.1\right)\right] \times 10^{-3} \tag{22}$$
$$\beta = 1.0$$

Till now, the prediction model of compressive strength degradation under the effect of frost damage was finally proposed, as shown in Eq. (21) and (22). Relative compressive strength Rf_c was used in this model to eliminate the effect from different shapes and sizes of the specimens (see **Table 1**). To verify the reliability of the model, the analytical damaged compressive strengths calculated by Eq. (21) and (22) were compared with several experimental results, as shown in **Fig. 7**, in which satisfactory agreement could be found. This fact strongly demonstrates the applicability of the proposed model.

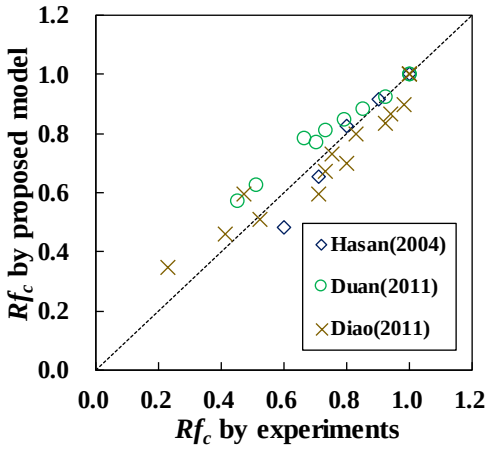

Fig. 7. Comparison of relative compressive strength by proposed model and experiments

In addition to the compressive strength, the elastic modulus (E_{cd}) and compressive strain at peak stress (ε_{cd}) of frost-damaged concrete were also important factors when evaluating the compressive behaviors. Several researches had suggested that the damaged elastic modulus and compressive strain at peak stress could be related to the relative compressive strength Rf_c [36-38]. As a result, the simulated values of relative elastic modulus RE_c ($=E_{cd}/E_c$) and relative compressive strain at peak stress $R\varepsilon_c$ ($=\varepsilon_{cd}/\varepsilon_c$) were plotted versus the relative compressive strength Rf_c in **Fig. 8(a) and (b)**. Empirical formulas by mathematical regression were developed to calculate RE_c and $R\varepsilon_c$ based on the relative compressive strength Rf_c, as shown in Eq. (23). **Fig. 9(a) and (b)** showed the comparison between Eq. (23) and available experimental data, where good correlations were found for both RE_c and $R\varepsilon_c$, which further proved the reliability of the simulation results as well as the proposed models [2-4, 7, 10, 13, 39].

$$RE_c = 1.284^{2.932 \cdot Rf_c} - 1.081$$
$$R\varepsilon_c = -1.261 Rf_c + 2.261 \tag{23}$$

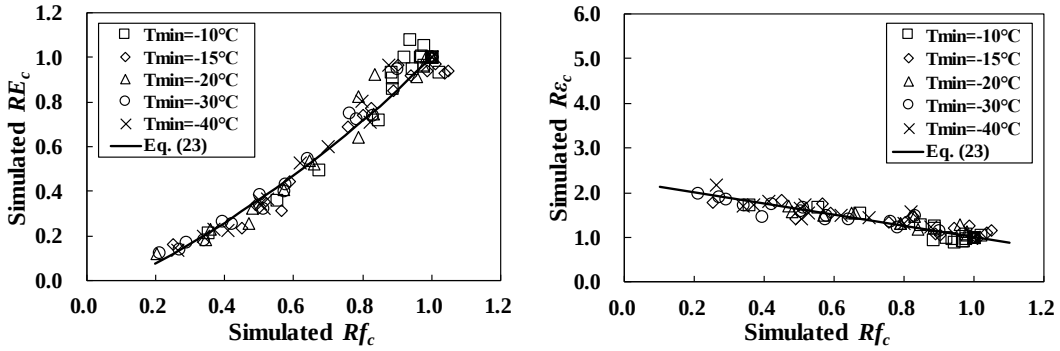

Fig. 8. Relationships between (a) RE_c and (b) $R\varepsilon_c$ versus Rf_c by RBSM simulation

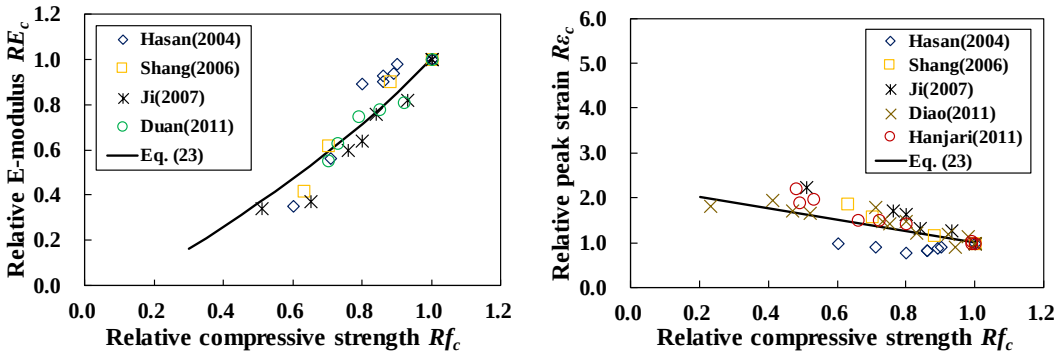

Fig. 9. Comparisons of (a) RE_c and (b) $R\varepsilon_c$ between proposed models and experiments

4.3 Degradation of tensile behaviors

In addition to compressive behaviors, the tensile strength of frost damaged concrete was also analyzed and modeled with the simulation results by RBSM. **Fig. 10** showed the tensile stress-strain curves of C0.5-20 series after suffering different numbers of FTC, the cracking failure pattern and deformation at post peak. In **Fig. 10**, the short red lines meant that the strains of normal springs had reached ε_{max} which made the normal springs ineffective (see **Fig. 3** and **4**) and the deformation had been enlarged by 50 times.

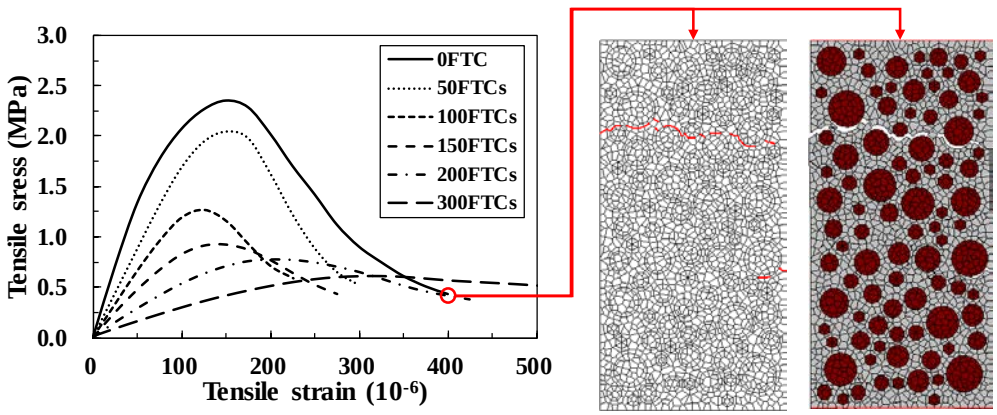

Fig. 10. Stress-strain relationship for C0.5-20 series, crack failure pattern and deformation

For non-damaged concrete, the relationship between compressive strength and tensile strength had been established by several standards, such as fib Model Code 2010 and Euro Code 2 etc. [40, 41]. For frost damaged concrete, such relationship had not yet been developed. However, some studies indicated the deteriorated tensile strength could be calculated by the damaged compressive strength and proposed empirical models with experimental results [36, 37]. Similarly, the simulated results between compressive and tensile strength of frost damaged concrete were plotted in **Fig. 11**. It could be found the tensile strength would have a higher diminishing than the compressive strength, which had also been reported in many previous studies [13, 22]. Through fitting the simulation data in **Fig. 11**, the model to calculate relative tensile strength Rf_t was proposed in Eq. (24). Comparison was made between the analytical and experimental results, in which good agreement could be achieved as shown in **Fig. 12** [4, 42].

$$Rf_t = 0.89e^{3.13(Rf_c-1)} + 0.11 \quad (24)$$

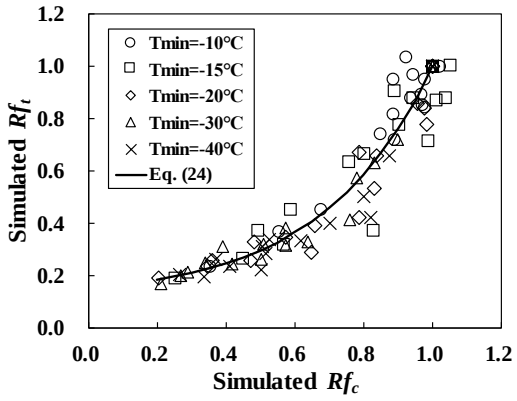

Fig. 11. Relationships between Rf_t versus Rf_c by RBSM simulation

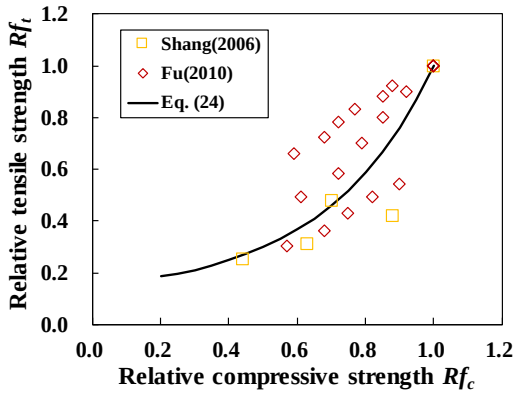

Fig. 12. Comparison of Rf_t between proposed model and experiments

4.4 Modeling of damaged constitutive relationship

4.4.1 Compressive stress-strain curve

Many mathematical equations had been developed on the complete compressive stress-strain relationship of sound concrete. As stated in section 4.2, the ascending branch of compressive stress-strain curve for frost damaged concrete was subjected to a change of stiffness, which was

believed by the randomly oriented cracks in the concrete due to frost damage before mechanical loading. Thus, the compressive loading would start with concrete of low stiffness before the closing of cracks, and then the loading would continue with a stiffer (still lower than the sound value) concrete [22, 36]. In order to consider such effect, a stress-strain relationship developed by Guo et al. was adopted to model the full compressive constitutive law for frost damaged concrete [7-9, 37, 43]. The model was expressed as following Eq. (25):

$$y=\begin{cases} ax+(3-2a)x^2+(a-2)x^3, 0\le x\le 1 \\ \dfrac{x}{b(x-1)^2+x}, x\ge 1 \end{cases} \tag{25}$$

where $y=\sigma/f_{cd}$ and $x=\varepsilon/\varepsilon_{cd}$; σ and ε represented the compressive stress and strain; a and b were independent parameters to control the shape of the ascending branch and descending branch, which could be adopted as Guo et al. [43]. The model was flexible with these shape controlling factors which could show the stiffness recovery effect. To calculate the parameters a_d and b_d for frost damaged concrete, Duan et al. suggested using the damaged compressive strength as index while Zou et al. and Cao et al. suggested adopting relative dynamic elastic modulus [7-9]. To unify their experimental results, here the relative compressive strength was utilized to calculate the parameters a_d and b_d. As drawn in **Fig. 13(a) and (b)**, the models to calculate the normalized ascending/descending shape controlling factors Ra ($=a_d/a$) and Rb ($=b_d/b$) could be given by regression from the experimental data, see Eq. (26).

$$\begin{aligned} Ra &= 0.167+0.833(Rf_c)^{3.512} \\ Rb &= 2.507-1.507(Rf_c)^{2.715} \end{aligned} \tag{26}$$

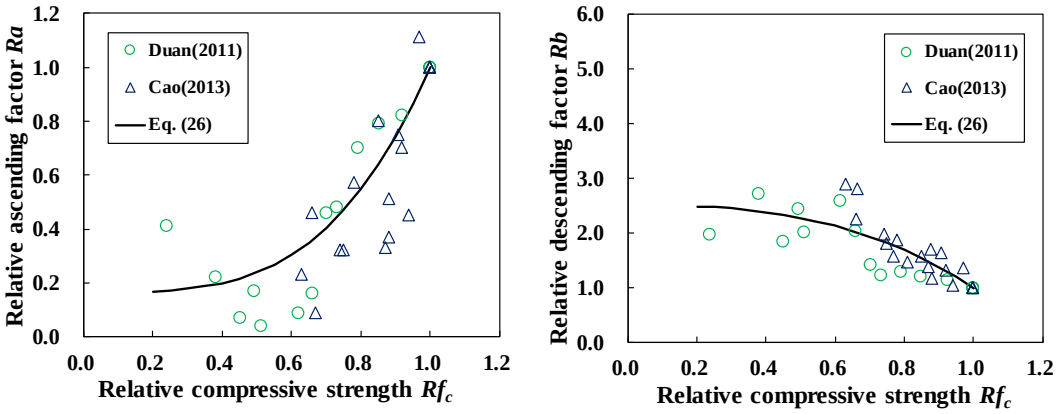

Fig. 13. Relationships between relative compressive strength and (a) Ra_d (b) Rb_d

Till now, the complete compressive stress-strain relationship had been proposed based on RBSM simulation results and experimental data. Firstly, the damaged compressive strength and strain at peak compressive stress could be calculated according to Eq. (21) and (23) while the damaged shape controlling parameters could be calculated as Eq. (26). Substitute the results into Eq. (25) gave the complete compressive stress-strain relationship for frost-damaged concrete. To investigate the proposed constitutive relationship, experimental results by Hanjari et al. was compared with the analytical results, see **Fig. 14** [13]. In **Fig. 14**, "EXP." and "CAL." represented

for the experimental and calculated results where satisfactory agreements were found.

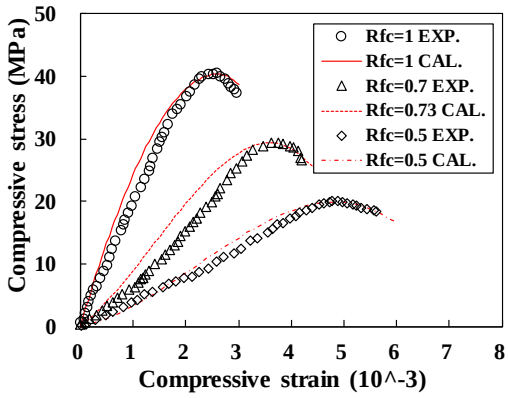

Fig. 14. Comparison between experimental and analytical compressive stress-strain curves

4.4.2 Tensile stress-strain curve

In the tensile constitutive model, the crack was assumed to propagate when tensile stress had reached the tensile strength [44]. As a results, the entire tensile stress-strain curve was divided into two parts: for pre-peak branch where tensile stress had not yet reached the tensile strength, linear behavior was adopted where the frost damaged tensile strength and stiffness could be calculated according to Eq. (24) and (23); for post-peak branch where tensile stress had reached the tensile strength and crack initiated, a simplified bi-linear relationship was proposed in the model based on test results by Hanjari et al., which could be easily utilized in the FEM application [13]. That is, if drawing a σ_t/f_{td} versus $w/w_{d\max}$ curve, the inflection point of this curve would be (0.14, 0.17), see Eq. (28). In which, σ_t and ε_t were tensile stress and strain; ε_{td} could be calculated as f_{td}/E_d; w and $w_{d\max}$ stood for the crack width and maximum crack width for frost-damaged concrete where $w_{d\max}$ could be calculated by fitting Hasan et al.'s and Hanjari et al.'s experimental data in spite of large scattering, see Eq. (27) and **Fig. 15** [13, 44]. $w_{\max}$ was the maximum crack width which could be measure in the laboratory test (0.8mm and 0.2mm for Hasan et al. and Hanjari et al.) [13, 44]. The analytical post-peak model was also illustrated together with Hasan et al.'s tested results, see **Fig. 16**. It could be indicated that the tension-softening curve proposed in Eq. (28) had a good correlation with the experimental results [44].

$$w_{d\max} = w_{\max} \times 6.716e^{-1.821Rf_t} \tag{27}$$

$$\begin{aligned} &\sigma_t = E_d \varepsilon_t, \varepsilon_t \le \varepsilon_{td} \\ &\frac{\sigma_t}{f_{td}} = 1 - 5.929\frac{w}{w_{d\max}}, \varepsilon_t \ge \varepsilon_{td} \ \&\ \frac{w}{w_{d\max}} \le 0.14 \\ &\frac{\sigma_t}{f_{td}} = 0.198\left(1 - \frac{w}{w_{d\max}}\right), \varepsilon_t \ge \varepsilon_{td} \ \&\ \frac{w}{w_{d\max}} > 0.14 \end{aligned} \tag{28}$$

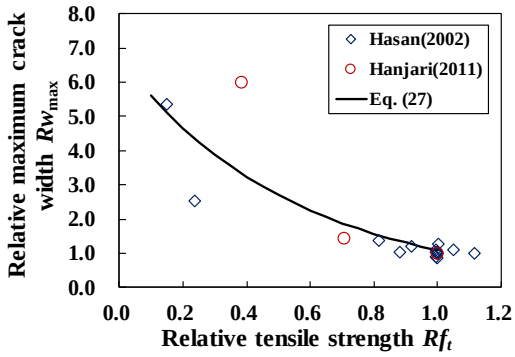

Fig. 15. Relationships between relative tensile strength and Rw_{dmax}

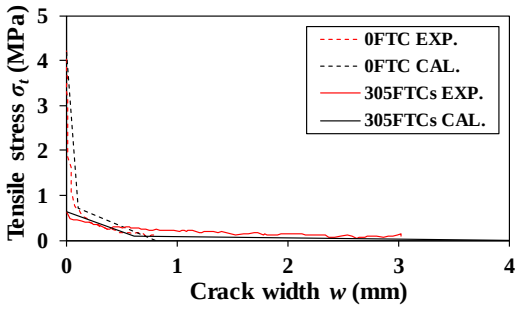

Fig. 16. Comparison between experimental and analytical tension softening curves

5. Conclusions

(1) A two-dimensional mesoscale numerical approach (RBSM) was adopted to analyze and model the mechanical behaviors of concrete under the effect of frost damage. The simulation results showed that the frost action had significant influence on both compressive and tensile behaviors of concrete as observed in previous experiments.

(2) On the basis of the simulation results, a prediction model for compressive strength of frost-damaged concrete was proposed according to water cement ratio, minimum temperature and number of freezing thawing cycles. Using normalized compressive strength as the damage index, other deteriorated properties such as tensile strength, elastic modulus and compressive strain at peak stress were also empirically modeled. All the analytical results had satisfactory correlations with existing experimental data which demonstrated the reliability and applicability of the models.

(3) Compressive and tensile stress-strain relationships of frost-damaged concrete were developed based on several experimental results, which can be applied to the prediction of structural behaviors of RC structures under the effect of frost damage through Finite Element Analysis approach.

Acknowledgements

The authors would like to express their sincere thanks to the MEXT (Ministry of Education, Culture, Sports, Science and Technology) scholarship for supporting the doctoral study and research work. The Grant-in-Aid for Scientific Research (A) of Japan Society of Promotion of Science (No. 26249064) is also greatly appreciated.

References

[1] American Society for Testing and Materials Committee, Standard test method for resistance of concrete to rapid freezing and thawing (ASTM C666-84), 1987 Annual Book of ASTM Standards. 4 (2) (1987).

[2] S. Shi, Effect of freezing-thawing cycles on mechanical properties of concrete, China Civil Engineering Journal. 30 (4) (1997) 35-42.

[3] M. Hasan, H. Okuyama, H. Sato, T. Ueda, Stress-strain model of concrete damaged by freezing and thawing cycles, Journal of Advanced Concrete Technology. 2 (1) (2004) 89-99.

[4] H. Shang, Y. Song, Experimental study of strength and deformation of plain concrete under biaxial compression after freezing and thawing cycles, Cement and Concrete Research. 36 (10) (2006) 1857-1864.

[5] National standard of The People's Republic of China, Standard test methods for long term performance and durability of ordinary concrete (GBJ82-85), Peking: China Architectural and Building Press. (1986).

[6] American Society for Testing and Materials Committee, Standard test method for resistance of concrete to rapid freezing and thawing (ASTM C666-97), West Conshohocken: ASTM International. (1997).

[7] A. Duan, W. Jin, J. Qian, Effect of freeze-thaw cycles on the stress-strain curves of unconfined and confined concrete, Materials and Structures. 44 (7) (2011) 1309-1324.

[8] C. Zou, J. Zhao, F. Liang, Stress-strain relationship of concrete in freeze-thaw environment, Frontiers of Architecture and Civil Engineering in China. 2 (2) (2008) 184-188.

[9] D. Cao, L. Fu, Z. Yang, X. Qin, Study of constitutive relations of compresses concrete subjected to action of freezing-thawing cycles, Journal of Building Materials. 16 (1) (2013) 17-23.

[10] B. Diao, Y. Sun, S. Cheng, Y. Ye, Effects of mixed corrosion, freeze-thaw cycles, and persistent loads on behavior of reinforced concrete beams, Journal of Cold Regions Engineering. 25 (1) (2011) 37-51.

[11] L. Peterson, L. Lohaus, M.A. Polak, Influence of freezing-and-thawing damage on behavior of reinforced concrete elements, ACI Materials Journal. 104 (4) (2007) 369-378.

[12] M. J. Setzer, Capillary suction, internal damage and freeze-thaw test-reference method and alternative methods A and B (RILEM TC 176 IDC), Materials and Structures. 34 (2001) 515-525.

[13] K.Z. Hanjari, P. Utgenannt, K. Lundgren, Experimental study of the material and bond properties of frost-damaged concrete, Cement and Concrete Research. 41(3) (2011) 244-254.

[14] T.C. Powers, The air requirement of frost resistant concrete, Proceedings of Highway Research Board, 29 (1949) 184-211.

[15] G.W. Scherer, J. Valenza, Mechanisms of frost damage, Materials Science of Concrete. 7 (60) (2005) 209-246.

[16] O. Coussy, P.J. Monteiro, Poroelastic model for concrete exposed to freezing temperatures, Cement and Concrete Research. 38 (1) (2008) 40-48.

[17] F. Gong, E. Sicat, D. Zhang, T. Ueda, Stress analysis for concrete materials under multiple freeze-thaw cycles, Journal of Advanced Concrete Technology. 13 (3) (2015a) 124-134.

[18] F. Gong, Y. Wang, D. Zhang, T. Ueda, Mesoscale simulation of deformation for mortar and concrete under cyclic freezing and thawing stress, Journal of Advanced Concrete Technology. 13 (6) (2015b) 291-304.

[19] F. Gong, T. Ueda, Y. Wang, D. Zhang, Z. Wang, Mesoscale simulation of fatigue behavior of concrete materials damaged by freeze-thaw cycles, Construction and Building Materials. 144 (2017a) 702-716.
[20] Z. Wang, F. Gong, D. Zhang, H. Hayashida, T. Ueda, Mesoscale simulation of concrete behavior with non-uniform frost damage with verification by CT imaging, Construction and Building Materials. 157 (2017) 203-213.
[21] K. Nagai, Y. Sato, T. Ueda, Mesoscopic simulation of failure of mortar and concrete by 2D RBSM, Journal of Advanced Concrete Technology. 2 (3) (2004) 359-374.
[22] T. Ueda, M. Hasan, K. Nagai, Y. Sato, L. Wang, Mesoscale simulation of influence of frost damage on mechanical properties of concrete, Journal of Materials in Civil Engineering. 21 (6) (2009) 244-252.
[23] T. Kawai, New discrete models and their application to seismic response analysis of structures, Nuclear Engineering and Design. 48 (1) (1978) 207-229.
[24] J.E. Bolander Jr, S. Saito, Fracture analyses using spring networks with random geometry, Engineering Fracture Mechanics. 61 (5-6) (1998) 569-591.
[25] Y. Wang, F. Gong, D. Zhang, T. Ueda, Estimation of ice content in mortar based on electrical measurements under freeze-thaw cycle, Journal of Advanced Concrete Technology. 14 (2) (2016) 35-46.
[26] Y. Xi, Z.P. Bazant, H.M. Jennings, Moisture diffusion in cementitious materials Adsorption isotherms, Advanced Cement Based Materials. 1 (6) (1994) 248-257.
[27] Jr. J. Hagymassy, S. Brunauer, R. S. Mikhail, Pore structure analysis by water vapor adsorption: I. t-curves for water vapor, Journal of Colloid and Interface Science. 29 (3) (1969) 485-491.
[28] M. Hasan, H. Okuyama, T. Ueda, The damage mechanism strain induced in frost cycles of concrete, Proceedings of Japan Concrete Institute. 25 (1) (2003) 401-406.
[29] E. Sicat, F. Gong, D. Zhang, T. Ueda, Change of the coefficient of thermal expansion of mortar due to damage by freeze thaw cycles, Journal of Advanced Concrete Technology. 11 (12) (2013) 333-346.
[30] Z. Sun, G.W. Scherer, Effect of air voids on salt scaling and internal freezing temperatures, Cement and Concrete Research. 40 (2) (2010) 260-270.
[31] E. Sicat, F. Gong, T. Ueda, D. Zhang, Experimental investigation of the deformational behavior of the interfacial transition zone (ITZ) in concrete during freezing and thawing cycles, Construction and Building Materials. 65 (2014) 122-131.
[32] F. Gong, Y. Wang, T. Ueda, D. Zhang, Modeling and mesoscale simulation of ice-strengthened mechanical properties of concrete at low temperatures, Journal of Engineering Mechanics. 143 (6) (2017b) 04017022.
[33] F. Gong, K. Maekawa, Multi-scale simulation of freeze-thaw damage to RC column and its restoring force characteristics, Journal of Engineering Structures. 156 (2018) 522-536.
[34] L. Berto, A. Saetta, D. Talledo, Constitutive model of concrete damaged by freeze-thaw action for wvaluation of structure performance of RC elements, Construction and Building Materials. 98 (2015) 559-569.
[35] L. Berto, A. Saetta, D. Talledo, R. Vitaliani, Structural analyais of frost damaged concstructions of a coupled environmental-mechanical damage model, Proceedings of the Joint 11th World Congress on Computational Mechanics. Barcelona (2014) 904-915.

[36] K.Z. Hanjari, P. Kettil, K. Lundgren, Modelling the structural behavior of frost-damaged reinforced concrete structures, Structure and Infrastructure Engineering. 9 (5) (2013) 416-431.
[37] A. Li, S. Xu, Y. Wang, Effects of frost-damage on mechanical performance of concrete, Journal of Wuhan University of Technology-Mater. Sci. Ed. 32 (1) (2017) 129-135.
[38] Q. Qin, S. Zheng, L. Li, L. Dong, Y. Zhang, S. Ding, Experimental study and numerical simulation of seismic behavior for RC columns subjected to freeze-thaw cycles, Advances in Materials Science and Engineering. (2017).
[39] X. Ji, The experimental study and theoretical analysis on the mechanical performance of concrete and bond behavior between concrete and steel bar after freezing and thawing, Doctoral Dissertation. Dalian University of Technology (2007).
[40] International Federation for Structural Concrete, Fib model code for concrete structures 2010, Berlin: Ernst & Sohn. (2013).
[41] British Standards Institution, Eurocode 2: Design of concrete structures: British standard, London: BSi. (2008).
[42] L. Fu, Experimental study on the strength of concrete under uniaxial tensile load after freeze-thaw cycles, Master Dissertation. Yangzhou University (2010).
[43] Z. Guo, X. Shi, Reinforced concrete theory and analysis. Tsinghua University Press (2003).
[44] M. Hasan, K. Nagai, Y. Sato, T. Ueda, Tensile stress-crack model for plain concrete damaged by freezing and thawing action, Proceedings of Japan Concrete Institute. 24 (2) (2002) 109-114.